Cell Systems

Report

Lattice Light-Sheet Microscopy Multi-dimensional Analyses (LaMDA) of T-Cell Receptor Dynamics Predict T-Cell Signaling States

Graphical Abstract

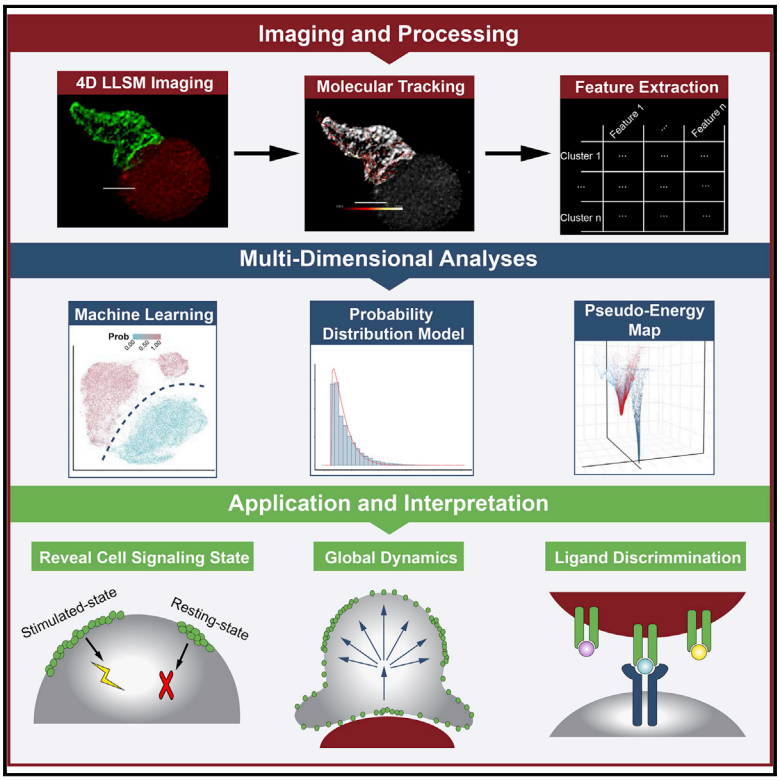

Highlights

- A pipeline for multi-dimensional analysis of lattice light-sheet microscopy data
- It applies machine learning techniques to enable subcellular signaling analyses
- It predicts different cell signaling states by surface molecular dynamics
- It enables T-cell receptor ligand discrimination

Authors

Jillian Rosenberg, Guoshuai Cao, Fernanda Borja-Prieto, Jun Huang

Correspondence

huangjun@uchicago.edu

In Brief

Lattice light-sheet microscopy multi-dimensional analyses (LaMDA) is a pipeline that combines high-spatiotemporal resolution four-dimensional lattice light-sheet microscopy, machine learning, and dimensionality reduction to analyze T-cell receptor (TCR) dynamics and predict T-cell signaling states without the need for complex biochemical measurements. We observe real-time global changes of TCRs across the 3D cell surface, differentiate stimulated cells from unstimulated cells, predict attenuated T-cell signaling after CD4 and CD28 receptor blockades, and discriminate between structurally similar TCR ligands.

Rosenberg et al., 2020, Cell Systems *10*, 433–444
May 20, 2020
https://doi.org/10.1016/j.cels.2020.04.006

CellPress

Cell Systems

CellPress
OPEN ACCESS

Report

Lattice Light-Sheet Microscopy Multi-dimensional Analyses (LaMDA) of T-Cell Receptor Dynamics Predict T-Cell Signaling States

Jillian Rosenberg,[1,3] Guoshuai Cao,[2,3] Fernanda Borja-Prieto,[2] and Jun Huang[1,2,4,*]
[1]Committee on Cancer Biology, University of Chicago, Chicago, IL 60637, USA
[2]Pritzker School of Molecular Engineering, University of Chicago, Chicago, IL 60637, USA
[3]These authors contributed equally
[4]Lead Contact
*Correspondence: huangjun@uchicago.edu
https://doi.org/10.1016/j.cels.2020.04.006

SUMMARY

Lattice light-sheet microscopy provides large amounts of high-dimensional, high-spatiotemporal resolution imaging data of cell surface receptors across the 3D surface of live cells, but user-friendly analysis pipelines are lacking. Here, we introduce lattice light-sheet microscopy multi-dimensional analyses (LaMDA), an end-to-end pipeline comprised of publicly available software packages that combines machine learning, dimensionality reduction, and diffusion maps to analyze surface receptor dynamics and classify cellular signaling states without the need for complex biochemical measurements or other prior information. We use LaMDA to analyze images of T-cell receptor (TCR) microclusters on the surface of live primary T cells under resting and stimulated conditions. We observe global spatial and temporal changes of TCRs across the 3D cell surface, accurately differentiate stimulated cells from unstimulated cells, precisely predict attenuated T-cell signaling after CD4 and CD28 receptor blockades, and reliably discriminate between structurally similar TCR ligands. All instructions needed to implement LaMDA are included in this paper.

INTRODUCTION

Lattice light-sheet microscopy (LLSM) is a recently developed microscopy technique that allows for four-dimensional (4D) (x, y, z, and time) imaging with exceptionally high temporal resolution (~100 frames/s, ~1 cell volume/s) and minimal photobleaching (Chen et al., 2014). LLSM provides high-dimensional, high spatiotemporal resolution imaging data of cell surface receptors or receptor microclusters ($\geq$1,000) over a long duration of time ($\geq$4 min) on the entire 3D surface of live primary cells. As a result of these capabilities, LLSM and other cutting-edge microscopy techniques generate larger and more complex high-dimensional data. These data are often underutilized due to a lack of comprehensive and efficient high-dimensional analysis pipelines that are accessible to the general user. The lack of such an analysis pipeline represents a key limitation in the use of imaging systems, including LLSM, that generate big data and are crucial to answering biological questions at the single-molecule level.

Here, we introduce lattice light-sheet microscopy multi-dimensional analyses (LaMDA), a pipeline to apply big data analysis techniques to high-dimensional LLSM data. LaMDA provides a complete end-to-end pipeline from upstream data collection and feature engineering to downstream machine learning and dimensionality reduction analyses. We intentionally constructed LaMDA using publicly available packages to enable easy adaptation and incorporation by general users to facilitate broad application across all areas of cell biology. Moreover, it was designed to motivate a paradigm shift wherein, rather than focusing on the cell as the unit of study, we focus on a molecular unit. The LaMDA pipeline supersedes the need for high-throughput collection of single-cell time-lapse data, which is difficult to capture using LLSM, by enabling extraction of sufficient molecular content for the use of high-dimensional analyses.

We applied LaMDA to image and analyze the dynamics of T-cell receptors (TCR) microclusters on the primary T-cell surface with high dimensionality to understand T-cell signaling states. T cells play a central role in adaptive immunity by mediating immune responses against cancer and infection (Janeway et al., 2001; Kahan et al., 2015; Thommen and Schumacher, 2018). As the dominant receptor, TCRs govern the recognition, activation, differentiation, and function of T cells in health and disease (Janeway et al., 2001; Kumar et al., 2018). Our LaMDA approach quantitatively revealed the global spatiotemporal dynamics of TCRs, reliably deciphered TCR microclusters from T cells at different signaling states, precisely identified the roles of co-stimulatory receptors, and accurately differentiated between T-cell stimulations triggered by structurally similar peptide ligands of different affinities. In addition to uncovering new T-cell biology, LaMDA can also be used to guide the pre-clinical design, development, and improvement of immunotherapies

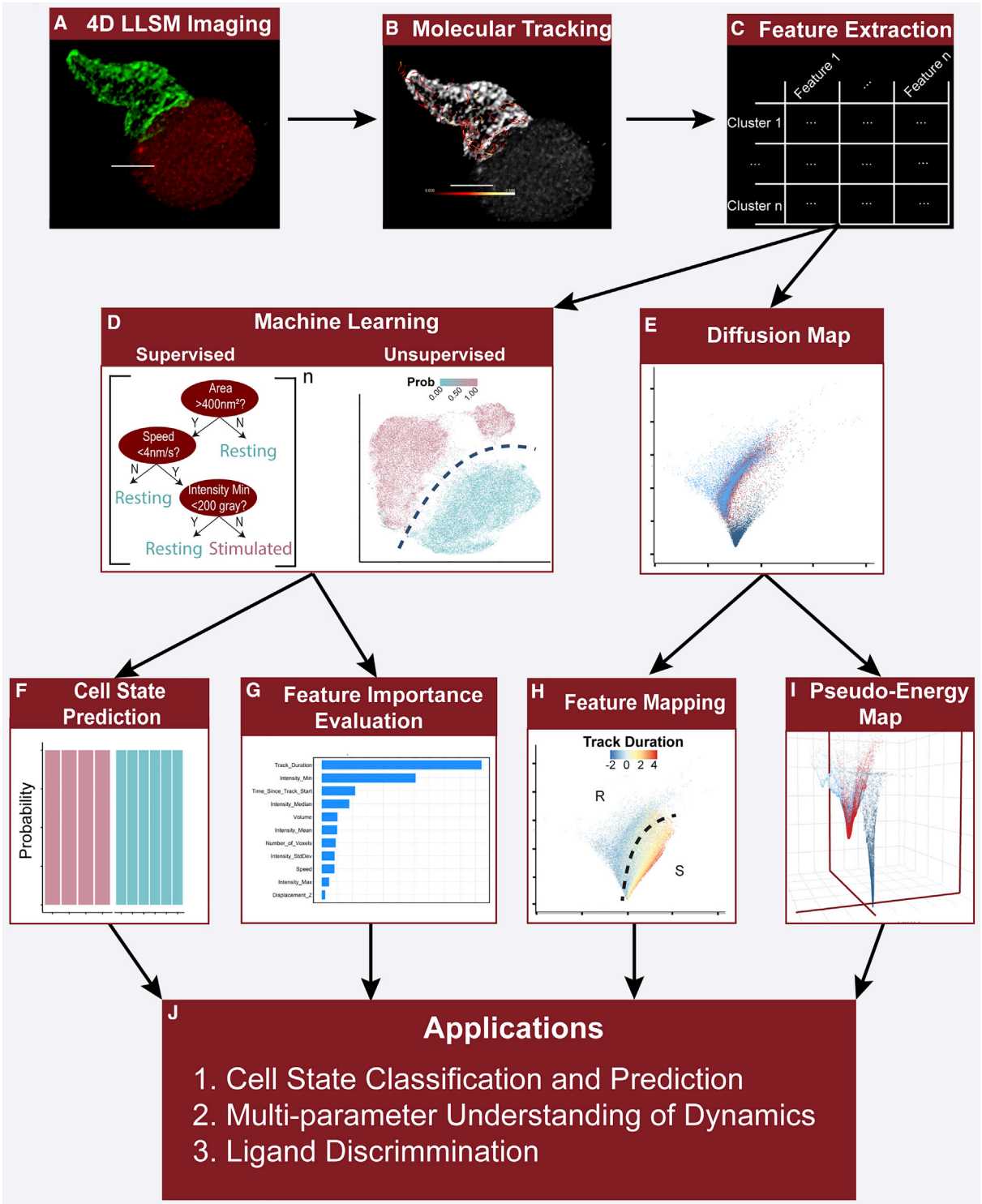

Figure 1. LaMDA Pipeline

(A) 4D imaging is conducted with LLSM. Receptors (green) on a cell are fluorescently labeled and 4D images are collected. Scale bar represents 5 μm.

(B) After deconvolution and debleaching, receptor microclusters are tracked with Imaris software. Scale bar represents 5 μm.

(C) Microcluster features are extracted from tracked TCR microclusters.

(D) Machine learning is conducted on extracted features for prediction. (Left) To classify between different cell states, supervised XGboost decision tree ensembles are trained as a binary classifier then tested and validated. (Right) Unsupervised UMAP clustering is used to independently validate the XGboost binary classifier. The XGboost binary classifier is used to predict the states of cells.

(legend continued on next page)

and vaccines for cancer, infection, and autoimmunity. Furthermore, as a flexible and broadly applicable pipeline, LaMDA provides a framework for future studies of other surface receptors or intracellular molecules on different cell types by directly linking molecular dynamics to cell signaling and function.

RESULTS

LaMDA

LaMDA was designed to enable big data analysis of high-dimensional LLSM data (Figure 1). To begin using LaMDA, LLSM is employed to capture single-cell images in four dimensions (x, y, z, and time) with high spatiotemporal resolution (~1 s/cell volume, x and y resolution ~200 nm, and z step 400 nm) (Figure 1A; Video S1). Then, advanced imaging software, such as Imaris, is utilized to track thousands of surface receptor microclusters (or other structures) from individual cells (Figure 1B) and extract multiple (36 in this study) statistical parameters for each tracked object simultaneously (Figure 1C). Due to the large size of collected datasets, machine learning and dimensionality reduction methods can be incorporated for analysis (Figures 1D and 1E). For example, a machine learning-based classifier (Chen and Guestrin, 2016) could be built to learn the inherently subtle yet very complex differences between the tracked receptors of two or more known cellular conditions. This classifier could then be used to predict the state of the receptor microclusters in new or less-understood cellular conditions (Figure 1F). Furthermore, feature importance metrics from the classifier can inform on the underlying biological differences in the system (Figure 1G). Once the classifier metrics are used to select important features, they can be studied individually by building statistical models. To understand if multiple parameters are working together to drive biological differences, dimensionality-reduction techniques, such as uniform manifold approximation and projection (UMAP) (McInnes et al., 2018) and diffusion maps (Coifman and Lafon, 2006; Ferguson et al., 2010), could be applied in parallel (Figures 1D and 1E) to graphically emphasize three important points: (1) these techniques cluster objects into several groups representative of different physical states; (2) the relative locations of these object states inform us on their relationships, indicating directionality and identifying the properties that change with that direction (Figure 1H); and (3) the local density at each coordinate on these dimensionality-reduction maps can be further transformed into a pseudo-energy surface to show relative stability of each object (Figure 1I). Together, LaMDA uses high-dimensional imaging and big data analyses to discover differentiating properties between cellular phenotypes and to reveal and predict underlying cellular states (Figure 1J).

LaMDA Discovers that TCR Microclusters Reflect T-Cell Activation State (Resting versus Stimulated), Not the Functional Phenotype (Naïve versus Blasting)

As a proof of concept of the LaMDA pipeline, we investigated the dynamics of TCRs, one of the most critical molecules in adaptive immunity and their relationship to T-cell activation. TCRs specifically recognize rare agonist peptide-major histocompatibility complexes (pMHCs) among numerous self-pMHCs on the surface of the cell being surveyed to trigger adaptive immune responses and therefore are essential molecules to combat infection and cancer (Chakraborty and Weiss, 2014; van der Merwe and Dushek, 2011). TCRs are known to form microclusters on the surface of the T cell and represent a key mechanism toward understanding T-cell signaling and function (Campi et al., 2005; Crites et al., 2014; Gagnon et al., 2012; Hashimoto-Tane et al., 2016, 2011; Hu et al., 2016; Huang et al., 2013; Hui et al., 2017; Lewis et al., 2018; Lillemeier et al., 2010; Murugesan et al., 2016; Roh et al., 2015; Sasmal et al., 2020; Schamel et al., 2005; Smoligovets et al., 2012; Taylor et al., 2017; Varma et al., 2006; Wang et al., 2019b; Yi et al., 2019; Yokosuka et al., 2005).

To visualize the 4D TCR microcluster dynamics by LLSM, we either fused a green fluorescent protein (GFP) to the C-terminus of the CD3ζ chain of the TCRs or used an Alexa Fluor 488 (AF488)-conjugated anti-TCRβ Fab to fluorescently label the TCRs at the membrane of live primary 5C.C7 $CD4^+$ T cells. Cytosolic mCherry-transduced CH27 cells were used as the antigen-presenting cells. After fluorescent labeling of TCRs on T cells and loading agonist moth cytochrome C (MCC) peptide onto the antigen-presenting cells, both the T cells and antigen-presenting cells were added to the LLSM imaging chamber for 4D imaging using 488- and 561-nm lasers. We recorded videos (4–6 min) of TCR microclusters across the entire 3D cell surface (x and y resolution ~200 nm, z step 400 nm, ~1 s/cell volume; Figures 2A–2D and S1A–S1G; Videos S1, S2, S3, S4, S5, S6 and S8) for four T-cell states: resting naïve, naïve stimulated by antigen-presenting cells, resting blasting, and blasting stimulated by antigen-presenting cells (Figure 2E).

We then tracked ~10,000 individual TCR microclusters on each T cell, measuring 36 parameters (including speed, direction, volume, intensity, area, location, and track duration; see STAR Methods for details) for each microcluster across the videos (Figures 2B, 2D, and S1K; Video S7). The data were pre-processed and an extreme gradient boosted (XGboost) decision tree ensemble (Chen and Guestrin, 2016) with logistic loss was built on 19 of these parameters (Figures 2F and S1H–S1K, referred to henceforth as the XGboost classifier) to classify TCR microclusters as microclusters from resting T cells or

(E) Diffusion maps are used as a dimensionality reduction technique to further quantify variations among cell states. The diffusion map is built from features selected based on their importance.
(F) The XGboost classifier is utilized to provide cell state predictions based on TCR microcluster features.
(G) The importance of each feature in the XGboost classifier is evaluated using SHAP, and the top feature is individually analyzed using appropriate statistical modeling.
(H) Diffusion map is colored by normalized features (e.g., track duration shown here). Dotted line indicates approximate divide between resting (R) and stimulated (S) cells.
(I) The diffusion map is transformed into a 3D pseudo-energy map by estimating local density of datapoints on the diffusion map. The 3D pseudo-energy map is used to analyze stability of tracked receptor microclusters across cell states.
(J) LaMDA pipeline applications, further detailed throughout paper.

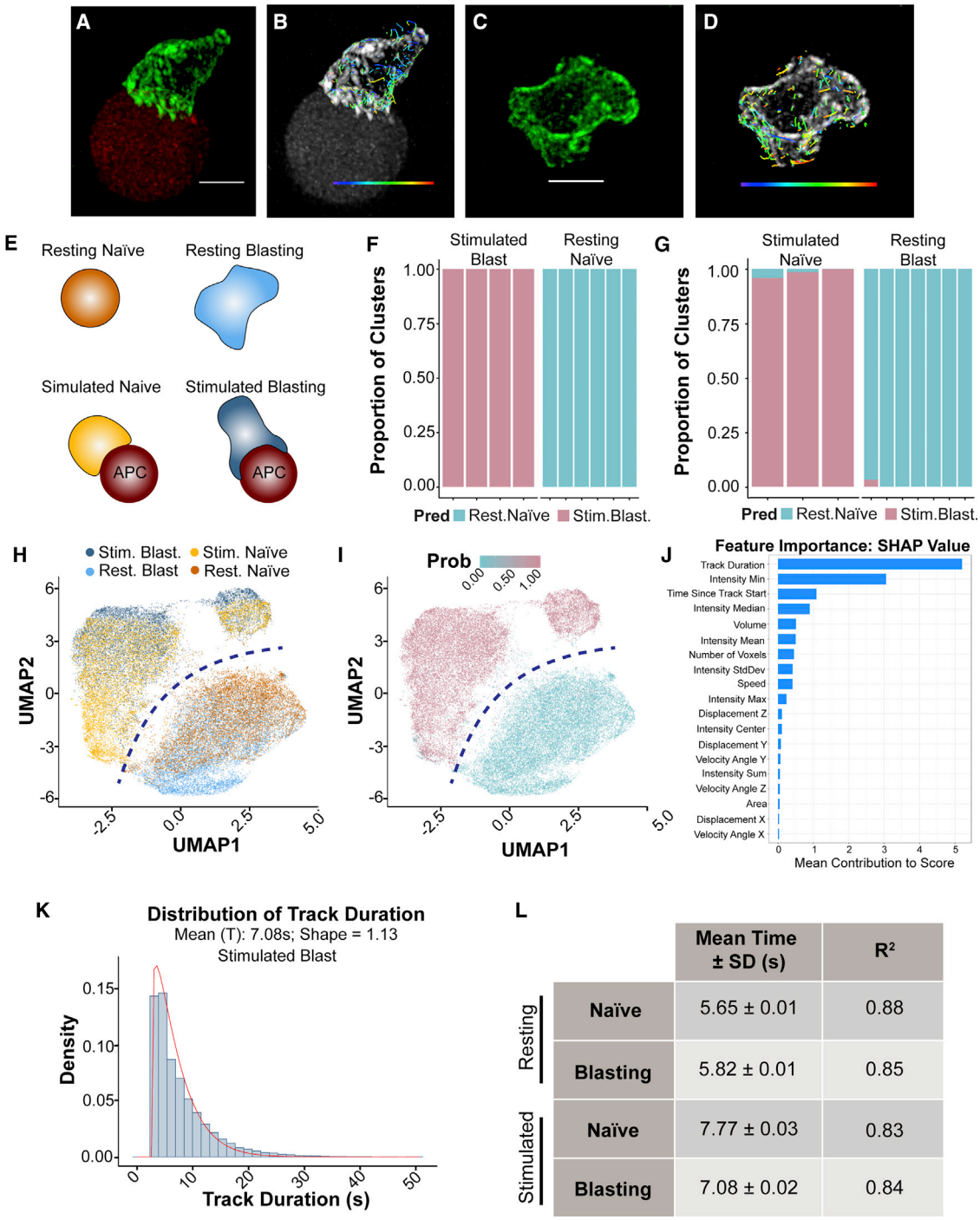

		Mean Time ± SD (s)	R^2
Resting	Naïve	5.65 ± 0.01	0.88
	Blasting	5.82 ± 0.01	0.85
Stimulated	Naïve	7.77 ± 0.03	0.83
	Blasting	7.08 ± 0.02	0.84

Figure 2. XGboost Binary Classifier Differentiates between T-Cell Signaling States

(A) 3D rendering of a blasting CD4$^+$ T cell stably transduced with CD3ζ-GFP (green) as it encounters a CH27 cell stably transduced with cytosolic mCherry (red). See also Video S1.

(B) Dragon tails showing particle positions over the previous eight frames overlaid onto (A). Color bar represents velocity angle X from 0° (purple) to 180° (red).

(C) 3D rendering of a blasting resting CD4$^+$ T cell stably transduced with CD3ζ-GFP (green). See also Video S2.

(D) Dragon tails showing particle positions over the previous eight frames overlaid onto (C). Color bar represents velocity angle X from 0° (purple) to 180° (red).

(E) Diagram depicting the four cell states, resting naïve, resting blasting, stimulated naïve, and stimulated blasting, graphically.

(F) XGboost training results. Each bar represents an independent cell (resting naïve cells n = 58,784 microclusters; stimulated blasting cells n = 97,237 microclusters). Pred, prediction. See also Figure S1K for number of microclusters in each cell.

(G) XGboost testing results. Each bar represents an independent cell (stimulated naïve cells, n = 38,809 microclusters; resting blasting cells, n = 60,116 microclusters). Pred, prediction. See also Figure S1K for number of microclusters in each cell.

(legend continued on next page)

stimulated T cells. To avoid strong correlation within the same cells, and to prevent the confounding effect of "past stimulation" (i.e., naïve versus blast), the XGboost classifier was first trained on microclusters from stimulated blast cells and resting naïve cells (Figure 2F). The classifier was later tested on stimulated naïve cells and resting blast cells (Figure 2G). Within the training set, a train-validate-test approach was utilized to avoid overfitting (see STAR Methods; Figure S1I). The XGboost classifier consists of 150 decision trees, each of which selects up to three parameters to fit a logistic regression model. The weighted values from all 150 trees are used to classify each microcluster (Figure S1H).

This classifier allows us to identify which observable features of TCR dynamics can function as signatures of a cell's state and allows for classification. For example, we hypothesized that because TCR microclusters behave differently in response to a stimulation (e.g., TCR-pMHC interaction) (Campi et al., 2005; Lillemeier et al., 2010; Varma et al., 2006; Yi et al., 2019), TCR microclusters switch from a "resting state" into a "stimulated state" and thus could be differentiated by machine learning. Indeed, in the internal test, the XGboost classifier could precisely differentiate between TCR microclusters on the resting naïve T cell from those on a stimulated blasting T cell with a validation accuracy of 100% and an internal test accuracy of 99.96% (Figure 2F). This suggests that our machine learning model can reliably predict the cell state, that is resting naïve versus stimulated blasting, by TCR microcluster dynamics alone. Accordingly, when a similar analysis was performed on two other T-cell states, stimulated naïve and resting blasting, we found large differences between TCR microcluster dynamics on stimulated and resting T cells, which allowed for accurate discrimination based on cell state by XGboost (Figure 2G). These results demonstrate that TCR microcluster dynamics are sufficient to predict cell state. Notably, however, the prediction of cell state is irrespective of prior antigen experience; the XGboost classifier could not distinguish between naïve and blasting T cells (Figures 2F and 2G). These results demonstrate that machine learning can precisely predict T cell signaling states (resting state versus stimulated state) using surface TCR dynamics, but that from the perspective of the TCR dynamics, naïve and blasting T cells are indistinguishable. This observation is not unique to the XGboost classifier. TCR microclusters can also be segregated into two groups, resting-state TCR microclusters and stimulated-state TCR microclusters, using the dimensionality reduction method, UMAP (McInnes et al., 2018) (Figures 2H and 2I, decision boundary in dark blue and Figure S2A).

Since the dynamic features of TCR microclusters represent a direct reflection of the T-cell signaling states, we next sought to use big data analysis techniques to investigate which biological features contributed to the observed differences. To further understand the features predicted by the XGboost classifier, we plotted the shapley additive explanations (SHAP) values (Lundberg and Lee, 2017a, 2017b) and found that track duration (i.e., the length of time a microcluster could be detected on the cell surface) was the most important feature (Figures 2J and S2B). While large SHAP values only directly indicate the features most informative to the decision trees, these features are often biologically relevant. Thus, we plotted the distribution of track duration for resting naïve, stimulated naïve, resting blasting, and stimulated blasting T cells and fitted three-parameter Weibull distribution models, a commonly used model for lifetime analyses (Lawless, 2002) (Figures 2K and S2C–S2F). The mean duration "T" was derived from the Weibull distributions (see STAR Methods) and describes the average lifetime of TCR microclusters on the surface of a T cell. We determined that antigen stimulation increased the mean duration of TCR microclusters significantly when compared with resting state, for both naïve and blasting T cells (Figures 2L and S2F). This implies a signaling pathway was initiated to alter global control of TCR microclusters on the surface.

Next, we characterized TCR microcluster dynamics using diffusion maps, a nonlinear dimensionality reduction technique that focuses on identifying the underlying manifold of the data and reveals diffusion-like behavior between different states (Coifman and Lafon, 2006; Ferguson et al., 2010). We sampled 8,000 microclusters from each cell group and chose a subset of 7 selected features (mean intensity, minimum intensity, intensity sum over the surface, area, volume, speed, and track duration) based on the XGboost classifier feature importance (as previously shown in Figure 2J) and their mutual independence (see STAR Methods). This diffusion map allowed us to graphically compare resting-state TCRs with stimulated-state TCRs (Figure 3A). We next estimated the local density of TCR microclusters on the diffusion map (Figure 3B) and derived the 3D pseudo-free energy surface (see STAR Methods) by adapting a method commonly used in molecular simulation research (Figure 3C) (Ferguson et al., 2010). For easy visualization and comparison, these 3D energy wells were projected along dimension 2 to become 2D energy wells (Figure 3D). Assuming all other terms that contribute to energy are held constant, the depth of the energy well directly revealed the stability of the TCR microclusters on each cell (Figure 3D).

We found the stimulated-state TCR microclusters occupy a much deeper energy well than the resting-state TCR microclusters, on both blasting and naïve T-cell surfaces (Figure 3D), demonstrating that, assuming all other terms that contribute to energy are held constant, TCR stimulation stabilizes TCR microclusters on the cell surface. We also analyzed the diffusion maps to compare individual dynamic features between resting and stimulated TCR microclusters (Figures 3E–3H, middle panel). For track duration, we found clear separation between resting-state and stimulated-state TCR microclusters in the diffusion

(H) UMAP of data from (F–G) with color indicating cell group. Boundary line represented in dark blue.
(I) UMAP of data from (F–G) with color indicating probability of microcluster to be a stimulated blasting microcluster as predicted by XGboost binary classifier. Probability was indicated by color scale (0.00–1.00). Boundary line represented in dark blue.
(J) SHAP values of each property of the microcluster in XGboost binary classifier.
(K) Weibull distribution fitting of microcluster track duration from stimulated blasting cells to obtain mean track duration. See also Figures S2C–S2F.
(L) Table of mean track duration for each cell group obtained by Weibull distribution fittings. Data are presented as mean ± standard deviation (SD) and the goodness of fit is indicated by R^2 values. Scale bars, 5 μm.

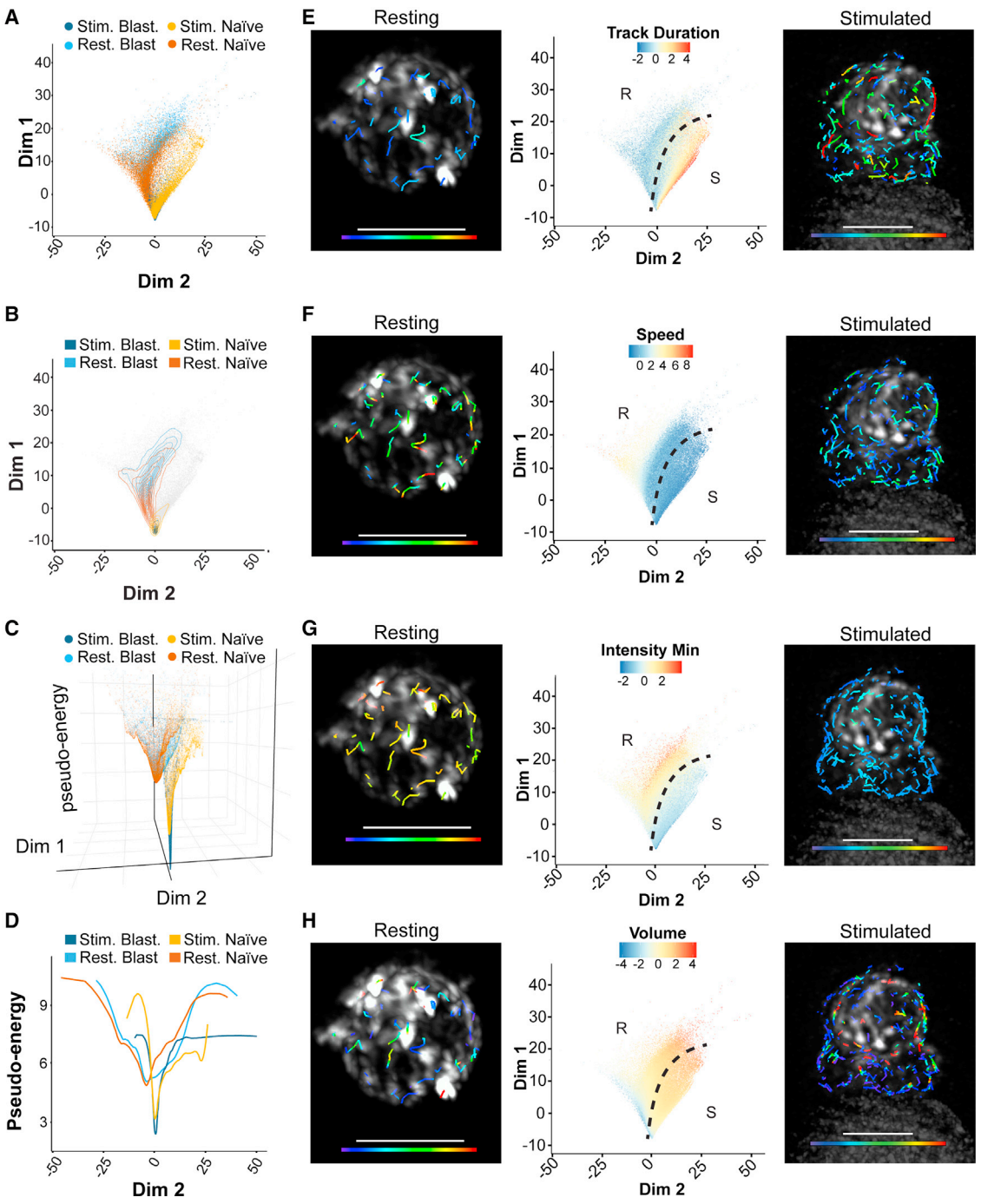

Figure 3. Diffusion Maps Differentiate between T-Cell Signaling States

(A) Diffusion map built from 7 selected features. Colors indicate cell group.

(B) Density map created by estimating local density on the diffusion map (A). Colors indicate cell group.

(C) Pseudo-energy map created from density map (B). Colors indicate cell group.

(D) Projection of pseudo-energy map (C) along dimension 2. Colors indicate cell group.

(E–H) Left: resting naïve cell from Figure S1A overlaid with dragon tails showing particle positions over the previous eight frames are color coded to show particle track duration from 0 s (purple) to 25 s (red) (E), particle speed from 0.0 μm/s (purple) to 0.5 μm/s (red) (F), particle intensity minimum from 0 AU (purple) to 500 AU (red) (G), or particle volume from 0.0 μm^2 (purple) to 0.2 μm^2 (red) (H). Center: diffusion map from Figure 3A colored by normalized track duration (E), speed (F), intensity minimum (G), or volume (H). Approximate boundary line between resting (R) and stimulated (S) cells (see also Figure 3A) represented in black. Right: Stimulated blasting cell from Figure S1D overlaid with dragon tails showing particle positions over the previous eight frames are color coded to show particle track duration from 0 s (purple) to 25 s (red) (E), particle speed from 0.0 μm/s (purple) to 0.5 μm/s (red) (F), particle intensity minimum from 0 AU (purple) to 500 AU (red) (G), or particle volume from 0.0 μm^2 (purple) to 0.2 μm^2 (red) (H).

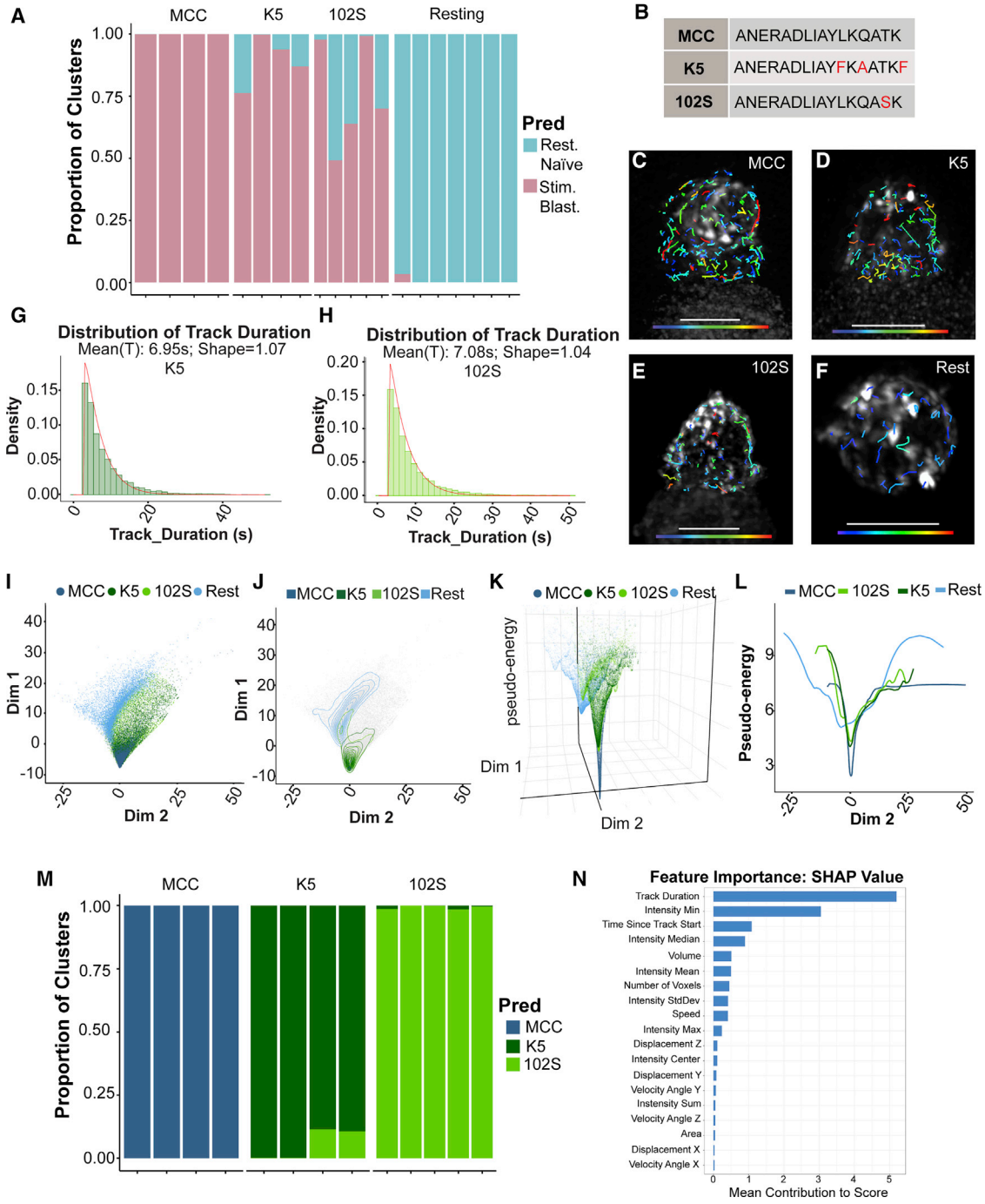

Figure 4. TCR Ligand Discrimination by LaMDA

(A) XGboost prediction results on microclusters from blasting cells stimulated with MCC (n = 97,237 microclusters), K5 (n = 24,786 microclusters), and 102S (n = 46,218 microclusters), and unstimulated resting cells (n = 58,784 microclusters). Each bar represents an independent cell. See also Figure S1K.

(B) Table of peptide sequences for MCC, K5, and 102S.

(C–F) 3D renderings of blasting cells stimulated with MCC (C), K5 (D), and 102S (E) and unstimulated resting blasting cells (F). All images are overlaid with dragon tails showing particle positions over the previous eight frames are color coded to show particle track duration (0–25 s). Scale bars, 5 μm.

(G and H) Weibull distribution fitting of microcluster track duration from blasting cells stimulated with K5 (G) or 102S (H). See also Figure S2F.

(I) Diffusion map built from the same selected features as Figure 3A, with colors indicating cell groups.

(J) Density map created from (I).

(legend continued on next page)

map (Figure 3E). Similar distinctions between resting-state and stimulated-state TCR microclusters were found for speed (Figure 3F) and minimum intensity (Figure 3G), whereas the differences in volume (Figure 3H) were less obvious. These analyses reinforced the reliability of our machine learning prediction. Spatially, we observed that the longest lasting microclusters (red) are not localized to the synapse as would be expected due to the TCR-pMHC bonds, but rather are dispersed throughout the whole cell (Figure 3E, right panel); similar global distributions were found for speed, minimum intensity, and volume (Figures 3F–3H, right panels), indicating that T cell activation is a global event.

Taken together, our data suggest that TCR microclusters directly reveal different signaling states of a T cell and support current biological understanding of TCR dynamics. It is known that TCR microcluster dynamics are closely linked with the actin network, which globally reorganizes with TCR-pMHC binding and signaling (Ritter et al., 2015; Billadeau et al., 2007; Bunnell et al., 2001; Fritzsche et al., 2017; Kumari et al., 2014; Roy and Burkhardt, 2018; Tsopoulidis et al., 2019; Valitutti et al., 1995). Accordingly, we observe that TCRs initially concentrated at the distal pole, quickly dispersed into small TCR microclusters and then continuously trafficked to the immunological synapse across the 3D spherical surface of the T cell (Figures S3A–S3D; Videos S5 and S6). Notably, after dividing the TCR microclusters between inside and outside synapse (Figures S3E–S3G), LaMDA was unable to identify differences between microclusters inside and outside the synapse (Figures S3H–S3J). This suggests that TCR triggering at the synapse propagates rapid, global re-organization of TCRs for effective antigen recognition and signaling. To our knowledge, such global, dynamic, and directional structural changes of TCR microclusters on the 3D T-cell surface had not yet been observed using conventional microscopy techniques or other biochemical or biophysical assays.

4D TCR Microcluster Dynamics Enable Ligand Discrimination

TCR ligand discrimination is essential for adaptive immunity. The dysfunction of TCR ligand discrimination can directly lead to cancer, infection, or autoimmunity. Moreover, TCR ligand discrimination displays two important characteristics: (1) high sensitivity—TCRs can recognize even a single agonist pMHC in the presence of abundant self-pMHCs (Huang et al., 2013; Irvine et al., 2002); and (2) high specificity—TCRs can discriminate between structurally similar peptides and elicit distinct immune responses (Alam et al., 1996; Huang et al., 2010; Kersh et al., 1998). Despite its critical importance, the molecular mechanism of TCR ligand discrimination remains controversial (van der Merwe and Dushek, 2011). A common problem is that most existing mechanistic models were proposed based on *in vitro* studies that often cannot reliably predict physiological events *in vivo*. One example is that the high-affinity, slow off-rate, and high-potency (as defined by *in vitro* measurements) K5 peptide triggers attenuated *in vivo* T-cell responses (Corse et al., 2010), and such experimental data cannot be explained by the prevailing kinetic models that were built based on *in vitro* binding affinity and/or half-life (Chakraborty and Weiss, 2014; Corse et al., 2010; van der Merwe and Dushek, 2011). In order to overcome the limitations imposed by *in vitro* studies, we applied our LaMDA approach to study TCR ligand discrimination to evaluate whether it can accurately predict physiological *in vivo* T-cell responses.

First, we confirmed that our experimental setup accurately reflects well-understood TCR biology by recapitulating previous observations of TCR's co-receptor CD4, a monomeric polypeptide that plays an important role in augmenting TCR signaling through associated tyrosine kinase Lck (Rudd et al., 1988; van der Merwe and Davis, 2003; Veillette et al., 1988; Chen and Flies, 2013; Janeway et al.,1988; Janeway 1992), and CD28, a co-stimulatory receptor required to fully activate the T cells without causing apoptosis (Boise et al., 1995; Esensten et al., 2016; Linsley and Ledbetter, 1993; Jenkins et al., 1988; Mueller et al., 1989). As expected, we observed that CD4 blockade (and Lck inhibition) and CD28 blockade impairs entry into the full stimulated state and significantly reduces the stability of TCR microclusters (Figures S4A–S4N and S2F). These observations support the conclusion that using LaMDA for observations of TCR dynamics, diverse signaling states can be identified without the need for complex biochemical or functional assays. Next, we measured the TCR microcluster dynamics stimulated by three structurally similar peptides K5, MCC, and 102S using LLSM (Figure 4B) (Corse et al., 2010). We then applied the same XGboost classifier trained on MCC-stimulated versus unstimulated TCR microclusters to this dataset. The XGboost classifier predicted that ~89.3% and ~76.1% of the microclusters stimulated by variants K5 and 102S, respectively, are in the stimulated state (Figure 4A). This indicates that both K5 and 102S stimulations resulted in partial activation, consistent with previous *in vivo* studies, which showed that both K5 and 102S peptides resulted in attenuated immune responses compared with the MCC peptide (Corse et al., 2010). Consistent with machine learning, we found that the Weibull-derived average lifetimes of 102S- and K5-stimulated microclusters were similar to those of MCC-stimulated microclusters but significantly different from those of resting microclusters (Figures 4C–4H and S2F).

To systematically study TCR ligand discrimination, we plotted a diffusion map of the TCR microclusters stimulated by the three structurally similar peptides K5, MCC, and 102S (Figures 4I and 4J). After converting the diffusion map to 3D (Figure 4K) and 2D (Figure 4L) energy wells, we were able to clearly visualize different activation states of T cells. Compared with the resting-state T cells without stimulation (blue), MCC-mediated stimulation (dark blue) induced the formation of the most stable TCR microclusters, while K5 (dark green) and 102S (green) resulted in less stable TCR microclusters. Our findings are well

(K) 3D pseudo-energy map created from (J) of blasting cells stimulated with MCC, K5, and 102S peptides, and resting blasting cells, with colors indicating cell groups.
(L) Projection of pseudo-energy map from (K) along dimension 2.
(M) Separate XGboost classifier built to differentiate microclusters from cells stimulated with MCC, K5, or 102S.
(N) SHAP values of each feature as used in XGboost binary classifier in (M).

aligned with a previous *in vivo* study by Allison and colleagues showing that the MCC peptide, rather than the K5 and 102S, triggers the optimal intracellular signaling, cytokine production, and cell proliferation (Corse et al., 2010).

Additionally, to fully test whether we can apply machine learning to TCR ligand discrimination, we trained another XGboost softmax classifier to distinguish between the TCR microclusters on T cells stimulated by MCC, K5, and 102S. We found that this alternative machine learning approach could be used to precisely differentiate between the TCR microcluster organization following stimulation by the three structurally similar peptides with ~96% accuracy (for training, validation, and test datasets) (Figures 4M and 4N). We expect our LaMDA pipeline can be extended to a wide range of ligand discrimination systems and detect subtle yet important dynamic differences between cell states, which provides a more physiologically relevant approach to study immune molecules and cells in cancer, infection, and autoimmunity.

DISCUSSION

We developed a modular pipeline, LaMDA, that combines high resolution 4D LLSM data with machine learning and dimensionality reduction techniques to analyze TCR microcluster dynamics and predict T-cell signaling states. In contrast to many studies that emphasize differences between naïve and blasting T cells, our LaMDA pipeline identified that the dynamics and distribution of TCR microclusters were primarily determined by the T-cell activation state (resting versus stimulated), rather than by prior antigen exposure (naïve versus blasting) (Figures 2 and 3). Using LaMDA, we also demonstrated that, assuming all other terms that contribute to energy are held constant, TCR-pMHC ligation stabilizes TCR microclusters globally across the entire T-cell surface (Figure S3), which has largely been overlooked in the past. Finally, we demonstrated that the same pipeline can be extended to study ligand discrimination (Figure 4).

In this study, we found that both K5- and 102S-mediated stimulation of T cells resulted in partial activation when compared with MCC (Figure 4). Our observations complement *in vivo* studies that have shown the K5 peptide results in attenuated immune responses compared with the MCC peptide (Corse et al., 2010) but stand in contrast to *in vitro* studies that have previously shown that K5 is a super-agonist with the highest TCR affinity and results in the strongest activation of T cells among three peptides (Corse et al., 2010; Li et al., 2004; Rabinowitz et al., 1996; Reay et al., 1994). This suggests that unlike common *in vitro* approaches, our LaMDA pipeline may be able to predict *in vivo* peptide potency in activating T cells and could be extended toward the development of peptide vaccines to treat infection, cancer, and autoimmunity (Hos et al., 2018; Li et al., 2014) or be used to study thymic education and/or peripheral tolerance, two very important topics in T-cell biology.

LLSM has been widely used across many biological fields to address a variety of questions (Cai et al., 2017; Chen et al., 2014; Condon et al., 2018; David et al., 2019; Ellefsen and Parker, 2018; Fritz-Laylin et al., 2017; Gao et al., 2019; McArthur et al., 2018; Mir et al., 2018a, 2018b; O'Shaughnessy et al., 2019; Phillips et al., 2019; Ritter et al., 2015). While LLSM has revealed important insights, current analysis approaches are not capable of considering all of the collected data to maximize the biological understanding or conclusions that could be drawn from the data. Most analysis approaches employed for investigating cell biology primarily focus on single features, such as intensity, colocalization, autocorrelation, diffusion rates, resolution, or directional analyses (Thorn, 2016; van der Merwe and Davis, 2003). The LaMDA pipeline is able to take full advantage of the 4D (x, y, z, and time) data intrinsically provided by LLSM and utilizes it in a myriad of advanced high-dimensional analysis tools, such as dimensionality reduction techniques and machine learning. However, LLSM is a low-throughput method regarding cell number, and if each cell is treated as a single data point, sufficient numbers for high-dimensional analysis methods cannot be reached. Thus, by considering individual molecules (e.g., TCRs) on the cell surface as opposed to single cells captured by LLSM, we are able to provide sufficient data points in a high-throughput manner to utilize these methods. By enacting the paradigm shift from single cell to single molecule in LLSM, the utility of data produced can be maximized.

In addition to surface molecules, this pipeline can still be used to track intracellular or recycling molecules. The analysis pipeline presented here could simply be used to address different questions. For example, LLSM has already been used to image and track T-cell granzymes, which are cell-death-inducing molecules packaged in intracellular vesicles and delivered to the surface of a target cell (Ritter et al., 2015). Our analysis pipeline therefore could analyze the tracks of these vesicles and address trafficking rates or directions. While any molecular label can be easily implemented, a large number of fluorescently detectable molecular units must exist in the biological system, highlighting an important consideration in implementing LaMDA for other studies.

Finally, LaMDA was intentionally designed to utilize existing tools and algorithms to perform complex multi-dimensional analysis, thereby enabling easy accessibility for any biologist without the need for familiarity with data science techniques. Moreover, while we used Imaris for feature extraction and an XGboost classifier for machine learning, this pipeline is highly modular and can be adapted for a variety of biological systems by incorporating alternative algorithms. Other machine learning techniques with different algorithms (e.g., XGboost or supportive vector machine), architectures (e.g., decision trees or neural network) or tasks (e.g., classification, segmentation, or detection) can be incorporated to substitute the XGboost classifier. In addition, multiple dimensionality reduction techniques are applicable (e.g., tSNE, PCA, etc.), and should be chosen based on desired purpose. Similarly, features do not have to be pre-defined and extracted from a software such as Imaris; rather, researchers could engineer context-specific features useful to their own research questions. Therefore, we anticipate broad usage of LaMDA to maximize biological understanding from LLSM data.

STAR★METHODS

Detailed methods are provided in the online version of this paper and include the following:

- KEY RESOURCES TABLE
- RESOURCE AVAILABILITY
  - Lead Contact
  - Materials Availability

SUPPLEMENTAL INFORMATION

Supplemental Information can be found online at https://doi.org/10.1016/j.cels.2020.04.006.

ACKNOWLEDGMENTS

We thank Dr. Vytas Bindokas and Dr. Christine Labno at the Integrated Light Microscopy Core Facility at the University of Chicago for supporting and maintaining the lattice light-sheet microscope and whose support to J.R. far exceeds scientific input. We thank the University of Chicago's Research Computing Center for providing the high-performance computing resources. We thank Dr. Enfu Hui and Dr. Yunlong Zhao for their contribution of mCherry-transduced CH27 cells. We thank Dr. Hans Schrieber and Dr. Yanran He for their contribution of CD3ζ-GFP cell transductions. We thank Ali Rahman for his extensive work in making figures. We thank Dr. Nicholas Ankenbruck and Dr. Enfu Hui for providing invaluable advice on our manuscript. We thank Howard Hughes Medical Institute, Janelia Research Campus for access to lattice light-sheet post-processing utility (LLSpy). This work was supported by NIH New Innovator award 1DP2AI144245 and NSF Career award 1653782 (to J.H.). J.R. is supported by the NSF Graduate Research Fellowships Program (DGE-1746045).

AUTHOR CONTRIBUTIONS

Conceptualization, J.R. and J.H. with input from G.C.; Methodology, J.R. and F.B.-P. with input from J.H. and G.C.; Formal Analysis G.C. with input from J.R. and J.H.; Writing, J.R., G.C., and J.H.; Supervision, J.H.

DECLARATION OF INTERESTS

The authors declare no competing interests.

Received: October 18, 2019
Revised: February 29, 2020
Accepted: April 21, 2020
Published: May 20, 2020

REFERENCES

Alam, S.M., Travers, P.J., Wung, J.L., Nasholds, W., Redpath, S., Jameson, S.C., and Gascoigne, N.R. (1996). T-cell-receptor affinity and thymocyte positive selection. Nature *381*, 616–620.

Billadeau, D.D., Nolz, J.C., and Gomez, T.S. (2007). Regulation of T-cell activation by the cytoskeleton. Nat. Rev. Immunol. *7*, 131–143.

Boise, L.H., Minn, A.J., Noel, P.J., June, C.H., Accavitti, M.A., Lindsten, T., and Thompson, C.B. (1995). CD28 costimulation can promote T cell survival by enhancing the expression of Bcl-XL. Immunity *3*, 87–98.

Bunnell, S.C., Kapoor, V., Trible, R.P., Zhang, W., and Samelson, L.E. (2001). Dynamic actin polymerization drives T cell receptor-induced spreading: a role for the signal transduction adaptor LAT. Immunity *14*, 315–329.

Cai, E., Marchuk, K., Beemiller, P., Beppler, C., Rubashkin, M.G., Weaver, V.M., Gérard, A., Liu, T.L., Chen, B.C., Betzig, E., et al. (2017). Visualizing dynamic microvillar search and stabilization during ligand detection by T cells. Science *356*, eaal3118.

Campi, G., Varma, R., and Dustin, M.L. (2005). Actin and agonist MHC-peptide complex-dependent T cell receptor microclusters as scaffolds for signaling. J. Exp. Med. *202*, 1031–1036.

Chakraborty, A.K., and Weiss, A. (2014). Insights into the initiation of TCR signaling. Nat. Immunol. *15*, 798–807.

Chen, B.C., Legant, W.R., Wang, K., Shao, L., Milkie, D.E., Davidson, M.W., Janetopoulos, C., Wu, X.S., Hammer, J.A., 3rd, Liu, Z., et al. (2014). Lattice light-sheet microscopy: imaging molecules to embryos at high spatiotemporal resolution. Science *346*, 1257998.

Chen, L., and Flies, D.B. (2013). Molecular mechanisms of T cell co-stimulation and co-inhibition. Nat. Rev. Immunol. *13*, 227–242.

Chen, T., and Guestrin, C. (2016). XGBoost: a scalable tree boosting system. arXiv, arXiv:1603.02754v3.

Coifman, R.R., and Lafon, S. (2006). Diffusion maps. Applied and Computational Harmonic Analysis *21*, 5–30.

Condon, N.D., Heddleston, J.M., Chew, T.L., Luo, L., McPherson, P.S., Ioannou, M.S., Hodgson, L., Stow, J.L., and Wall, A.A. (2018). Macropinosome formation by tent pole ruffling in macrophages. J. Cell Biol. *217*, 3873–3885.

Corse, E., Gottschalk, R.A., Krogsgaard, M., and Allison, J.P. (2010). Attenuated T cell responses to a high-potency ligand in vivo. PLoS Biol. *8*, e1000481.

Crites, T.J., Padhan, K., Muller, J., Krogsgaard, M., Gudla, P.R., Lockett, S.J., and Varma, R. (2014). TCR Microclusters pre-exist and contain molecules necessary for TCR signal transduction. J. Immunol. *193*, 56–67.

David, A.F., Roudot, P., Legant, W.R., Betzig, E., Danuser, G., and Gerlich, D.W. (2019). Augmin accumulation on long-lived microtubules drives amplification and kinetochore-directed growth. J. Cell Biol. *218*, 2150–2168.

Ellefsen, K.L., and Parker, I. (2018). Dynamic Ca^{2+} imaging with a simplified lattice light-sheet microscope: a sideways view of subcellular Ca^{2+} puffs. Cell Calcium *71*, 34–44.

Esensten, J.H., Helou, Y.A., Chopra, G., Weiss, A., and Bluestone, J.A. (2016). CD28 costimulation: from mechanism to therapy. Immunity *44*, 973–988.

Ferguson, A.L., Panagiotopoulos, A.Z., Debenedetti, P.G., and Kevrekidis, I.G. (2010). Systematic determination of order parameters for chain dynamics using diffusion maps. Proc. Natl. Acad. Sci. USA *107*, 13597–13602.

Fritz-Laylin, L.K., Riel-Mehan, M., Chen, B.C., Lord, S.J., Goddard, T.D., Ferrin, T.E., Nicholson-Dykstra, S.M., Higgs, H., Johnson, G.T., Betzig, E., and Mullins, R.D. (2017). Actin-based protrusions of migrating neutrophils are intrinsically lamellar and facilitate direction changes. eLife *6*, e26990.

Fritzsche, M., Fernandes, R.A., Chang, V.T., Colin-York, H., Clausen, M.P., Felce, J.H., Galiani, S., Erlenkämper, C., Santos, A.M., Heddleston, J.M., et al. (2017). Cytoskeletal actin dynamics shape a ramifying actin network underpinning immunological synapse formation. Sci. Adv. *3*, e1603032.

Gagnon, E., Schubert, D.A., Gordo, S., Chu, H.H., and Wucherpfennig, K.W. (2012). Local changes in lipid environment of TCR microclusters regulate membrane binding by the CD3epsilon cytoplasmic domain. J. Exp. Med. *209*, 2423–2439.

Gao, R., Asano, S.M., Upadhyayula, S., Pisarev, I., Milkie, D.E., Liu, T.L., Singh, V., Graves, A., Huynh, G.H., Zhao, Y., et al. (2019). Cortical column and whole-brain imaging with molecular contrast and nanoscale resolution. Science *363*, eaau8302.

Hashimoto-Tane, A., Sakuma, M., Ike, H., Yokosuka, T., Kimura, Y., Ohara, O., and Saito, T. (2016). Micro-adhesion rings surrounding TCR microclusters are essential for T cell activation. J. Exp. Med. *213*, 1609–1625.

Hashimoto-Tane, A., Yokosuka, T., Sakata-Sogawa, K., Sakuma, M., Ishihara, C., Tokunaga, M., and Saito, T. (2011). Dynein-driven transport of T cell receptor microclusters regulates immune synapse formation and T cell activation. Immunity *34*, 919–931.

Hos, B.J., Tondini, E., van Kasteren, S.I., and Ossendorp, F. (2018). Approaches to improve chemically defined synthetic peptide vaccines. Front. Immunol. *9*, 884.

Hu, Y.S., Cang, H., and Lillemeier, B.F. (2016). Superresolution imaging reveals nanometer- and micrometer-scale spatial distributions of T-cell receptors in lymph nodes. Proc. Natl. Acad. Sci. USA *113*, 7201–7206.

Huang, J., Brameshuber, M., Zeng, X., Xie, J., Li, Q.J., Chien, Y.H., Valitutti, S., and Davis, M.M. (2013). A single peptide-major histocompatibility complex ligand triggers digital cytokine secretion in CD4(+) T cells. Immunity *39*, 846–857.

Huang, J., Zarnitsyna, V.I., Liu, B., Edwards, L.J., Jiang, N., Evavold, B.D., and Zhu, C. (2010). The kinetics of two-dimensional TCR and pMHC interactions determine T-cell responsiveness. Nature *464*, 932–936.

Hui, E., Cheung, J., Zhu, J., Su, X., Taylor, M.J., Wallweber, H.A., Sasmal, D.K., Huang, J., Kim, J.M., Mellman, I., and Vale, R.D. (2017). T cell costimulatory receptor CD28 is a primary target for PD-1-mediated inhibition. Science *355*, 1428–1433.

Irvine, D.J., Purbhoo, M.A., Krogsgaard, M., and Davis, M.M. (2002). Direct observation of ligand recognition by T cells. Nature *419*, 845–849.

Janeway, C.A., Jr. (1992). The T cell receptor as a multicomponent signalling machine: CD4/CD8 coreceptors and CD45 in T cell activation. Annu. Rev. Immunol. *10*, 645–674.

Janeway, C.A., Jr., Carding, S., Jones, B., Murray, J., Portoles, P., Rasmussen, R., Rojo, J., Saizawa, K., West, J., and Bottomly, K. (1988). CD4+ T cells: specificity and function. Immunol. Rev. *101*, 39–80.

Janeway, C.A., Travers, P., Walport, M., and Shlomchik, M.J. (2001). Immunobiology: The Immune System in Health and Disease, Fifth Edition (Garland Publishing).

Jenkins, M.K., Ashwell, J.D., and Schwartz, R.H. (1988). Allogeneic non-T spleen cells restore the responsiveness of normal T cell clones stimulated with antigen and chemically modified antigen-presenting cells. J. Immunol. *140*, 3324–3330.

Kahan, S.M., Wherry, E.J., and Zajac, A.J. (2015). T cell exhaustion during persistent viral infections. Virology *479–480*, 180–193.

Kersh, G.J., Kersh, E.N., Fremont, D.H., and Allen, P.M. (1998). High- and low-potency ligands with similar affinities for the TCR: the importance of kinetics in TCR signaling. Immunity *9*, 817–826.

Kumar, B.V., Connors, T.J., and Farber, D.L. (2018). Human T cell development, localization, and function throughout life. Immunity *48*, 202–213.

Kumari, S., Curado, S., Mayya, V., and Dustin, M.L. (2014). T cell antigen receptor activation and actin cytoskeleton remodeling. Biochim. Biophys. Acta *1838*, 546–556.

Lawless, J.F. (2002). Statistical Models and Methods for Lifetime Data, Second Edition (Wiley-Interscience).

Leisegang, M., Engels, B., Schreiber, K., Yew, P.Y., Kiyotani, K., Idel, C., Arina, A., Duraiswamy, J., Weichselbaum, R.R., Uckert, W., et al. (2016). Eradication of large solid tumors by gene therapy with a T-cell receptor targeting a single cancer-specific point mutation. Clin. Cancer Res. *22*, 2734–2743.

Lewis, J.B., Scangarello, F.A., Murphy, J.M., Eidell, K.P., Sodipo, M.O., Ophir, M.J., Sargeant, R., Seminario, M.C., and Bunnell, S.C. (2018). ADAP is an upstream regulator that precedes SLP-76 at sites of TCR engagement and stabilizes signaling microclusters. J. Cell Sci. *131*, jcs215517.

Li, Q.J., Dinner, A.R., Qi, S., Irvine, D.J., Huppa, J.B., Davis, M.M., and Chakraborty, A.K. (2004). CD4 enhances T cell sensitivity to antigen by coordinating Lck accumulation at the immunological synapse. Nat. Immunol. *5*, 791–799.

Li, W., Joshi, M.D., Singhania, S., Ramsey, K.H., and Murthy, A.K. (2014). Peptide vaccine: progress and challenges. Vaccines (Basel) *2*, 515–536.

Lillemeier, B.F., Mörtelmaier, M.A., Forstner, M.B., Huppa, J.B., Groves, J.T., and Davis, M.M. (2010). TCR and Lat are expressed on separate protein islands on T cell membranes and concatenate during activation. Nat. Immunol. *11*, 90–96.

Linsley, P.S., and Ledbetter, J.A. (1993). The role of the CD28 receptor during T cell responses to antigen. Annu. Rev. Immunol. *11*, 191–212.

Lundberg, S., and Lee, S. (2017a). A unified approach to interpreting model predictions. arXiv, arXiv:1705.07874v2.

Lundberg, S.M., and Lee, S. (2017b). Consistent feature attribution for tree ensembles. arXiv, arXiv:1706.06060v6.

McArthur, K., Whitehead, L.W., Heddleston, J.M., Li, L., Padman, B.S., Oorschot, V., Geoghegan, N.D., Chappaz, S., Davidson, S., San Chin, H., et al. (2018). BAK/BAX macropores facilitate mitochondrial herniation and mtDNA efflux during apoptosis. Science *359*, eaao6047.

McInnes, L., Healy, H., and Melville, J. (2018). UMAP: uniform manifold approximation and projection for dimension reduction. arXiv, arXiv:1802.03426v2.

Mir, M., Reimer, A., Stadler, M., Tangara, A., Hansen, A.S., Hockemeyer, D., Eisen, M.B., Garcia, H., and Darzacq, X. (2018a). Single molecule imaging in live embryos using lattice light-sheet microscopy. Methods Mol. Biol. *1814*, 541–559.

Mir, M., Stadler, M.R., Ortiz, S.A., Hannon, C.E., Harrison, M.M., Darzacq, X., and Eisen, M.B. (2018b). Dynamic multifactor hubs interact transiently with sites of active transcription in Drosophila embryos. eLife *7*, e40497.

Mueller, D.L., Jenkins, M.K., and Schwartz, R.H. (1989). An accessory cell-derived costimulatory signal acts independently of protein kinase C activation to allow T cell proliferation and prevent the induction of unresponsiveness. J. Immunol. *142*, 2617–2628.

Murugesan, S., Hong, J., Yi, J., Li, D., Beach, J.R., Shao, L., Meinhardt, J., Madison, G., Wu, X., Betzig, E., and Hammer, J.A. (2016). Formin-generated actomyosin arcs propel T cell receptor microcluster movement at the immune synapse. J. Cell Biol. *215*, 383–399.

O'Shaughnessy, E.C., Stone, O.J., LaFosse, P.K., Azoitei, M.L., Tsygankov, D., Heddleston, J.M., Legant, W.R., Wittchen, E.S., Burridge, K., Elston, T.C., et al. (2019). Software for lattice light-sheet imaging of FRET biosensors, illustrated with a new Rap1 biosensor. J. Cell Biol. *218*, 3153–3160.

Phillips, J.K., Sherman, S.A., Cotton, K.Y., Heddleston, J.M., Taylor, A.B., and Finan, J.D. (2019). Characterization of neurite dystrophy after trauma by high speed structured illumination microscopy and lattice light sheet microscopy. J. Neurosci. Methods *312*, 154–161.

Rabinowitz, J.D., Beeson, C., Wülfing, C., Tate, K., Allen, P.M., Davis, M.M., and McConnell, H.M. (1996). Altered T cell receptor ligands trigger a subset of early T cell signals. Immunity *5*, 125–135.

Reay, P.A., Kantor, R.M., and Davis, M.M. (1994). Use of global amino acid replacements to define the requirements for MHC binding and T cell recognition of moth cytochrome c (93–103). J. Immunol. *152*, 3946–3957.

Ritter, A.T., Asano, Y., Stinchcombe, J.C., Dieckmann, N.M., Chen, B.C., Gawden-Bone, C., van Engelenburg, S., Legant, W., Gao, L., Davidson, M.W., et al. (2015). Actin depletion initiates events leading to granule secretion at the immunological synapse. Immunity *42*, 864–876.

Roh, K.H., Lillemeier, B.F., Wang, F., and Davis, M.M. (2015). The coreceptor CD4 is expressed in distinct nanoclusters and does not colocalize with T-cell receptor and active protein tyrosine kinase p56lck. Proc. Natl. Acad. Sci. USA *112*, E1604–E1613.

Rosenberg, J., and Huang, J. (2020). Visualizing surface T-cell receptor dynamics four-dimensionally using lattice light-sheet microscopy. J. Vis. Exp. *155*, e59914.

Roy, N.H., and Burkhardt, J.K. (2018). The actin cytoskeleton: a mechanical intermediate for signal integration at the immunological synapse. Front. Cell Dev. Biol. *6*, 116.

Rudd, C.E., Trevillyan, J.M., Dasgupta, J.D., Wong, L.L., and Schlossman, S.F. (1988). The CD4 receptor is complexed in detergent lysates to a protein-

tyrosine kinase (pp58) from human T lymphocytes. Proc. Natl. Acad. Sci. USA *85*, 5190–5194.

Sasmal, D.K., Feng, W., Roy, S., Leung, P., He, Y., Cai, C., Cao, G., Lian, H., Qin, J., Hui, E., et al. (2020). TCR-pMHC bond conformation controls TCR ligand discrimination. Cell. Mol. Immunol. *17*, 203–217.

Schamel, W.W., Arechaga, I., Risueño, R.M., van Santen, H.M., Cabezas, P., Risco, C., Valpuesta, J.M., and Alarcón, B. (2005). Coexistence of multivalent and monovalent TCRs explains high sensitivity and wide range of response. J. Exp. Med. *202*, 493–503.

Schindelin, J., Arganda-Carreras, I., Frise, E., et al. (2012). Fiji: an open-source platform for biological-image analysis. Nat. Methods *9*, 676–682.

Smoligovets, A.A., Smith, A.W., Wu, H.J., Petit, R.S., and Groves, J.T. (2012). Characterization of dynamic actin associations with T-cell receptor microclusters in primary T cells. J. Cell Sci. *125*, 735–742.

Taylor, M.J., Husain, K., Gartner, Z.J., Mayor, S., and Vale, R.D. (2017). A DNA-based T cell receptor reveals a role for receptor clustering in ligand discrimination. Cell *169*, 108–119.e20.

Thommen, D.S., and Schumacher, T.N. (2018). T cell dysfunction in cancer. Cancer Cell *33*, 547–562.

Thorn, K. (2016). A quick guide to light microscopy in cell biology. Mol. Biol. Cell *27*, 219–222.

Tsopoulidis, N., Kaw, S., Laketa, V., Kutscheidt, S., Baarlink, C., Stolp, B., Grosse, R., and Fackler, O.T. (2019). T cell receptor-triggered nuclear actin network formation drives CD4(+) T cell effector functions. Sci. Immunol. *4*, eaav1987.

Valitutti, S., Dessing, M., Aktories, K., Gallati, H., and Lanzavecchia, A. (1995). Sustained signaling leading to T cell activation results from prolonged T cell receptor occupancy. Role of T cell actin cytoskeleton. J. Exp. Med. *181*, 577–584.

van der Merwe, P.A., and Davis, S.J. (2003). Molecular interactions mediating T cell antigen recognition. Annu. Rev. Immunol. *21*, 659–684.

van der Merwe, P.A., and Dushek, O. (2011). Mechanisms for T cell receptor triggering. Nat. Rev. Immunol. *11*, 47–55.

Varma, R., Campi, G., Yokosuka, T., Saito, T., and Dustin, M.L. (2006). T cell receptor-proximal signals are sustained in peripheral microclusters and terminated in the central supramolecular activation cluster. Immunity *25*, 117–127.

Veillette, A., Bookman, M.A., Horak, E.M., and Bolen, J.B. (1988). The CD4 and CD8 T cell surface antigens are associated with the internal membrane tyrosine-protein kinase p56lck. Cell *55*, 301–308.

Wang, Q.L., Liang, J.Q., Gong, B.N., Xie, J.J., Yi, Y.T., Lan, X., and Li, Y. (2019b). T cell receptor (TCR)-induced PLC- γ 1 SUMOylation via PIASxbeta and PIAS3 SUMO E3 ligases regulates the microcluster assembly and physiological function of PLC- γ 1. Front. Immunol. *10*, 314.

Yi, J., Balagopalan, L., Nguyen, T., McIntire, K.M., and Samelson, L.E. (2019). TCR microclusters form spatially segregated domains and sequentially assemble in calcium-dependent kinetic steps. Nat. Commun. *10*, 277.

Yokosuka, T., Sakata-Sogawa, K., Kobayashi, W., Hiroshima, M., Hashimoto-Tane, A., Tokunaga, M., Dustin, M.L., and Saito, T. (2005). Newly generated T cell receptor microclusters initiate and sustain T cell activation by recruitment of Zap70 and SLP-76. Nat. Immunol. *6*, 1253–1262.

STAR★METHODS

KEY RESOURCES TABLE

REAGENT or RESOURCE	SOURCE	IDENTIFIER
Antibodies		
Alexa Fluor 488 anti-mouse TCR β chain Antibody	BioLegend	Cat# 109215; RRID: AB_493345
Purified anti-mouse CD4 Antibody	BioLegend	Cat#: 100401; RRID: AB_312686
Purified anti-mouse CD28 Antibody	BioLegend	Cat#: 102101; RRID: AB_312866
Purified anti-mouse anti-CD3ε	University of Chicago Monoclonal Antibody Facility	Clone 145-2C11; RRID: AB_312666
Chemicals, Peptides, and Recombinant Proteins		
RBC Lysis Buffer	eBioscience	Cat#: 00-4300-54
Moth Cytochrome C (MCC), sequence ANERADLIAYLKQATK	Elimbio	N/A
K5, sequence ANERADLIAYFKAATKF	Elimbio	N/A
102S, sequence ANERADLIAYLKQASK	Elimbio	N/A
Ficoll-Paque Plus	GE Healthcare	Cat#: 17-1440-02
Recombinant mouse IL-2	Sigma-Aldrich	Cat#: I0523
Poly-L-Lysine	Phenix Research Products	Cat#: P8920-100ML
PP2 (4-Amino-5-(4-chlorophenyl)-7-(t-butyl)pyrazolo[3,4-d]pyrimidine)	Millipore Sigma	Cat#: P0042
Retronectin	Clontech	Cat#: T100A
Recombinant human IL-2	Peprotech	Cat#: AF-200-02
Critical Commercial Assays		
MojoSort Mouse CD4 T Cell Isolation Kit	BioLegend	Cat#: 480033
Thermo Scientific Pierce Fab Micro Preparation Kits	Thermo Fisher Scientific	Cat#: 44685
Experimental Models: Cell Lines		
Mouse: CH27-mCherry	Laboratory of Dr. Enfu Hui	N/A
Experimental Models: Organisms/Strains		
Mouse: B10.A-Rag2-/- H2-T18a Tg (Tcra5CC7,Tcrb5CC7)	NIH	N/A
Recombinant DNA		
MIG-CD3ζ-GFP	Laboratory of Dr. Hans Schrieber	N/A
Software and Algorithms		
Slidebook	3i	https://www.intelligent-imaging.com/slidebook
Imaris	Oxford Instruments	https://imaris.oxinst.com/
LLSpy	LLSpy was used under license from Howard Hughes Medical Institute, Janelia Research Campus. Contact innovation@janelia.hhmi.org for access.	https://llspy.readthedocs.io/en/latest/
R	CRAN	https://www.r-project.org/
Fiji	Schindelin et al., 2012	https://imagej.net/Fiji
Deposited Data		
Raw data	This paper	https://doi.org/10.5281/zenodo.3743835
Other		
Lattice Light-Sheet Microscope	3i	N/A
5mm round coverslips	World Precision Instruments	Cat#: 502040

RESOURCE AVAILABILITY

Lead Contact

Further information and requests for reagents may be directed to, and will be fulfilled by, the corresponding author Jun Huang (huangjun@uchicago.edu).

Materials Availability

This study did not generate unique reagents.

Data and Code Availability

All data that support the findings of this study are available at the following link: https://doi.org/10.5281/zenodo.3743835.

EXPERIMENTAL MODEL AND SUBJECT DETAILS

5C.C7 TCR-transgenic RAG2 knockout mice in B10.A background aged 8-9 weeks were used in this study. Animals of both sexes were used and the influence of sex was not considered in the analysis of the data. All experiments were conducted according to protocols approved by the Institutional Animal Care and Use Committee of the University of Chicago.

METHOD DETAILS

Cell Culture

Cytosolic mCherry-transduced CH27 cells were a gift generously donated by Dr. Enfu Hui. To obtain blasting T cells, 5C.C7 mouse spleen was harvested and run through a 70 μm cell strainer with warm complete RPMI. Splenocytes were resuspended in 5 mL of RBC Lysis Buffer (Life Technologies) for 5 min, washed three times, and resuspended in 5 mL of complete RPMI. MCC peptide (ANERADLIAYLKQATK; 10 μM) was added to stimulate T-cell proliferation, and recombinant mouse IL-2 (100 U/mL, Sigma-Aldrich) was added the following day. Blasting T cells were used on days 6–10 after peptide pulsing. mCherry-CH27 cells and 5C.C7 blasting T cells were both maintained in complete medium (RPMI 1640 supplemented with 10% [v/v] FBS, 1% [v/v] Pen/Strep, L-glutamine [2 mM], 2-mercaptoethanol [50 μM]).

Cell Preparation

Cells were prepared as previously described (Rosenberg and Huang, 2020). Briefly, mCherry-CH27 cells were used as antigen presenting cells for imaging experiments. Dead mCherry-CH27 cells were first removed by Ficoll-Paque Plus (GE Healthcare, cat: 17-1440-03) density gradient centrifugation (centrifuged at 930 × g for 10 min at 4 °C, acc/dec: SLOW/SLOW). Live mCherry-CH27 cells were washed three times with complete medium, and then incubated with 10 μM K5 (ANERADLIAYFKAATKF), MCC (ANERADLIAYLKQATK) or 102S (ANERADLIAYLKQASK) for 3 h at 37 °C and 5% CO_2. Peptide-pulsed mCherry-CH27 cells were then washed three times and resuspended in imaging media (phenol red-free Leibovitz's L-15 medium supplemented with 10% [v/v] FBS, 1% [v/v] Pen/Strep, L-glutamine [2 mM]) for use.

Naïve T cells were prepared by negative isolation using 5C.C7 transgenic mouse spleens. Mouse splenocytes were prepared by Ficoll-Paque Plus (GE Healthcare, cat: 17-1440-03) density gradient centrifugation (centrifuged at 930 × g for 10 min at 4 °C, acc/dec: SLOW/SLOW) to remove dead cells. Naive $CD4^+$ T cells were then harvested by negative isolation (MojoSort Mouse CD4 T Cell Isolation Kit, BioLegend, cat: 480033). Cells were washed three times with complete medium and incubated with Alexa488-labeled anti-TCRβ (2 μg; clone H-57, Biolegend) antibody Fab for 30 min at 37 °C and 5% CO_2. After three washes, naïve T cells were resuspended in imaging media for use.

Day 6-10 blasting T cells were prepared by Ficoll-Paque Plus (GE Healthcare, cat: 17-1440-03) density gradient centrifugation (centrifuged at 930 × g for 10 min at 4 °C, acc/dec: SLOW/SLOW) to remove dead cells. Live blasting T cells were washed three times with complete medium and incubated with Alexa488-labeled anti-TCRβ (2 μg; clone H-57, Biolegend) antibody Fab for 30 min at 37 °C and 5% CO_2. After three washes, blasting T cells resuspended in imaging media for use.

CD3ζ-GFP Transduction

Primary 5C.C7 T cells were retrovirally transduced with CD3ζ-GFP according to a previously published method (Leisegang et al., 2016). Briefly, calcium phosphate precipitation was used to transfect MIG-CD3ζ-GFP vector into ecotropic platinum-E retroviral packaging cells. Supernatant containing virus was harvested after 48 and 72 h and filtered through 0.2 μm cellulose acetate membrane. Splenocytes isolated from 5C.C7 mice cultured in complete RPMI were stimulated with anti-CD3ε mAb (5 μg/mL; Clone 145-2C11, University of Chicago Monoclonal Antibody Facility), anti-CD28 mAb (0.5 μg/mL; Clone 37.51, Biolegend), and recombinant human IL-2 (40 U/mL; Peprotech). A 6-well plate was coated with Retronectin (12.5 μg/mL; Clontech) in PBS at 4 °C overnight, then centrifuged for 90 min at 3,000 x g with 2 mL of viral supernatant. Day 1 activated splenocytes were transferred to plate with viral supernatant, protamine sulfate (4 μg/mL) was added, and plate was centrifuged at 800 × g for 90 min. After 24 h, medium was replaced with fresh viral supernatant containing protamine sulfate (4 μg/mL), and plate was centrifuged at 800 × g for 90 min. After 16 h, transduction efficiency was determined by examining GFP fluorescence using flow cytometry.

Fab Preparation

All Fabs used in this study were prepared using a Micro Fab Preparation Kit (Thermo Fisher Scientific). Briefly, anti-TCRβ, anti-CD4, and anti-CD28 whole antibodies were prepared with desalting column, then digested with papain, a nonspecific thiol-endopeptidase, for 6 h on tabletop shaker at 37 °C. Digested Fabs were purified according to kit instructions. Fab purification was confirmed with SDS-PAGE gel electrophoresis.

Signaling Perturbation Assays

For PP2 assay, day 6-10 blasting T cells were pre-incubated with PP2 (10 μM; 4-Amino-5-(4-chlorophenyl)-7-(t-butyl)pyrazolo[3,4-d] pyrimidine; Sigma-Aldrich) for 1 h at 37 °C and 5% CO_2. Pre-treated cells were imaged at 37 °C and 5% CO_2 in the presence of 10 μM PP2.

For CD4 and CD28 blockade, an anti-CD4 (clone Gk1.5, BioLegend) or anti-CD28 (clone 37.51, BioLegend) Fab was prepared and purified with Micro Fab Preparation Kit (Thermo Fisher Scientific). Day 6-10 T cells were pre-incubated for 1 h at 37 °C and 5% CO_2 with anti-CD4 Fab (2 μg/mL) or anti-CD28 Fab (4 μg/mL) then imaged in the presence of 2 μg/mL Fab.

Lattice Light-sheet Microscopy

Version 2 of the Lattice Light Sheet Microscope (3i) was used for 4D imaging experiments. The LLSM was aligned daily according to manufacturer's instructions. LLSM bath was filled with imaging media and warmed to 37 °C. Round coverslips (5 mm) were prepared prior to imaging by incubation with 0.1% [w/v] solution of Poly-L-Lysine for 30 min. Poly-L-Lysine was aspirated, and coverslips were allowed to dry. To prepared coverslips were added 200,000 peptide-pulsed mCherry-CH27 cells. Cells were allowed to settle for 10 min before adhering to sample holder and placing in LLSM bath. T cells (200,000) were added dropwise to the LLSM bath above the coverslip and imaged immediately. Imaging was conducted with dither set to 3 and 10 ms exposures. Z-steps (60) were collected with a 0.4 μm step size. Cells were imaged for no more than one hour before exchanging with fresh cells.

QUANTIFICATION AND STATISTICAL ANALYSIS

Image Processing

Data were deskewed and deconvolved using LLSpy (cudaDeconv) software, used under license from Howard Hughes Medical Institute, Janelia Research Campus; collected point spread functions (PSF, collected under imaging conditions) were used to deconvolve, and 20 iterations were conducted. Bleach correction was conducted in ImageJ using histogram matching. Deskewed, deconvolved, and debleached videos were imported into Imaris (Bitplane) for rendering and tracking. Tracking TCR microclusters was conducted with the "surfaces" module using the Autoregressive Motion Expert tracking method; any two consecutive surfaces were allowed to move a maximum distance of 0.5 μm and disappear for no more than 3 frames to be considered on one track; watershed was not enabled. The surfaces module was also used to create a surface of the antigen presenting cell, and a distance map was made extending outward from the antigen presenting cell surface. Surface module statistics were exported for every TCR surface. Thus, for all following sections of the STAR Methods, "surfaces" or "surface modules" refer to the segmentation and tracking of TCR microclusters conducted by Imaris.

Data Preprocessing

For each cell, the raw surface module statistics from the TCR microcluster tracks were imported and processed in R as follows. All non-numerical or missing statistics values were removed. All statistical variables were then combined into a dataframe with rows as unique surface modules and columns as the different statistical variables, including track-specific variables. For the initial parameter extraction from Imaris, 36 variables out of 134 available parameters were collected (see Data Sharing and Availability for complete list). These variables were selected by refraining from fitting a certain shape to the surface unit, thus removing all shape-specific features such as "BoundingBoxAA Length" or "Ellipsoid axes". Additionally, only first-order measurements were included where first and second order are available, so as to minimize errors in tracking; for example, displacement XYZ was included, but not displacement^2, as any error in connecting the two surface units along the track would be propagated. As a separate example, all acceleration measurements were also excluded, as they depend on velocity measurements, which depend on the displacement. This would compound any "displacement error". Redundant features were preserved (such as standard deviation vs. variation of speed along track), as the XGboost classifier would only select one parameter to analyze at a time, thereby self-excluding the effect of redundant parameters. To normalize the dynamic range, all intensity-related variables (e.g., Mean Intensity, Max Intensity, Min Intensity, etc.) and all size-related variables (e.g., Area, Volume, Number of Voxels, etc.) were then log transformed.

XGboost Decision Trees Ensemble Binary Classifier

To build the classifier and make predictions, all data were further processed as follows. For each cell, 19 out of the 36 variables were selected as features of interest (see Data Sharing and Availability for complete list). In this subset, all track-specific (as opposed to surface-specific) parameters were removed in order to focus the decision tree on each surface (or TCR microcluster), rather than each track, as an individual unit. The only exception was Track Duration, which is important for lifetime distribution studies. For a series of surface modules that were assigned to the same track by Imaris, the track duration feature values were defined as the temporal length of that track (i.e., the same value for surface modules of the same track). In addition, position XYZ was removed, as the

position of a surface is always relative to the orientation of the cell in that particular video, therefore irrelevant to compare across videos. The chosen statistics from all microclusters on all cells were then pooled for each group to avoid bias on the biological variation from cell to cell. Surface modules with Mean Intensity (I_{mean}) values lower than mean(I_{mean})-1.5×IQR(I_{mean}) were removed as they are likely to be noise rather than a true surface module. Then, all statistics were standardized: $\frac{x-\bar{x}}{SD(x)}$.

The processed data were then used to train a binary classifier to differentiate between microclusters from resting cells and microclusters from stimulated cells as follows. Of the four groups of cell types, microclusters from stimulated blast T cells and resting naïve T cells were chosen to train the classifier, which was later tested on the stimulated naïve cells and resting blast cells. This division of cell types was chosen for two reasons: (1) to avoid any strong correlation within the same cells; and (2) to test against the confounding effect of "past stimulation" (i.e., naïve vs. blast). To build the classifier, a "train-test-validate" approach was used to avoid overfitting (Figure S1I). Thus, the processed data of stimulated blast T cells and resting naïve T cells were divided into a training set (75%; 117,066 surface modules), validation set (17.5%; 27,316 surface modules) and internal test set (7.5%; 11,705 surface modules). The binary classifier was built as a XGBoost logistic regression decision tree ensemble, using the caret package (v.6.0) in R, with 5-fold cross-validation and the following parameters: nrounds = 150; max_depth = 3; eta = 0.4; gamma = 0; colsample_bytree = 0.8; min_child_weight = 1; and subsample = 1. Feature importance was then assessed using the SHAP values extracted from the xgb.plot.shap function. All subsequent plots were constructed using the ggplot2 (v.3.2.0) and the ggpubr (v.0.2.1) package in R. Finally, the model was tested on every surface module (i.e., TCR microclusters) from new data (stimulated naïve and resting blast categories) to predict whether these TCR microclusters were from stimulated blast T cells or from resting naïve T cells. The final label was assigned to be the one with greater predicted probability (i.e., either stimulated blasting T cells or resting naïve T cells).

XGboost Decision Tree Ensemble Softmax Classifier

To differentiate multiple ligands, a separate multi-class XGboost classifier was constructed as follows. For each cell, the same 19 out of 36 variables as used for the initial XGboost Decision Tree Ensemble Binary Classifier were selected; however, a 20th variable, average distance to antigen presenting cell, was added. The last feature was not applicable to the binary classifier above because the resting cells do not encounter antigen presenting cells, but it is applicable to all classes here. Surface modules with Mean Intensity (I_{mean}) values lower than mean(I_{mean})-1.5×IQR(I_{mean}) were removed since they are likely to be noise rather than a true surface module. Then, all statistics were standardized: $\frac{x-\bar{x}}{SD(x)}$.

The processed data of microclusters from blasting T cells stimulated by MCC, 102S, and K5 were pooled and divided into a training set (75%; 126,254 surface modules), validation set (17.5%; 29,460 surface modules) and test set (7.5%; 12,623 surface modules). The softmax classifier was built as a XGBoost decision tree ensemble using softmax probabilities as the objective, using the caret package (v.6.0) in R, with 5-fold cross-validation and the following parameters: nrounds = 500; max_depth = 6; eta = 0.3; gamma = 0; colsample_bytree = 1; min_child_weight = 1; and subsample = 1. The final model was used to re-predict the probability of every surface module from the blasting T cells stimulated by MCC, 102S, and K5. The final label was assigned to be the peptide (MCC, 102S, or K5) with greatest predicted probability. Results were plotted using the ggplot2 (v.3.2.0) and the ggpubr (v.0.2.1) package in R.

Weibull Distribution

Weibull distribution (Lawless, 2002) is a commonly used statistical distribution that describes lifetime distribution. The three-parameter Weibull model we used is of the form:

$$f(T) = \frac{\beta}{\eta}\left(\frac{T-T_0}{\eta}\right)^{\beta-1}\exp\left(-\frac{T-T_0}{\eta}\right)^{\beta}$$

where:

$$T \geq 0;\ \eta>0;\ \beta>0$$

A Weibull distribution was used to fit the raw track duration values for each group using the WeibullR (v.1.0.10) package in R. The location (T_0), shape (β), and scale (η) parameters were extracted directly from the model. The mean life-time values were calculated as:

$$\overline{T} = T_0 + \eta \cdot \Gamma\left(\frac{1}{\beta}+1\right).$$

UMAP

Pre-processed data were separately processed as an independent validation of the XGboost classifier. For each cell, the same 19 out of the 37 variables as used for the XGboost classifier were selected as features of interest (see Data Sharing and Availability for complete list). The chosen statistics from all cells of all groups were then pooled for each group to avoid bias on the biological variation from cell to cell. Surface modules with Mean Intensity (I_{mean}) values lower than mean (I_{mean})-1.5×IQR (I_{mean}) were removed since they are likely to be noise rather than a true surface module. Then, all statistics were then standardized: $\frac{x-\bar{x}}{SD(x)}$. Then data of the groups of

interest were then pooled and used to build a UMAP (McInnes et al., 2018) using the uwot (v.0.1.3) package in R with parameters: min_dist = 0.1; n_neighbors = 25; all others set to default. All subsequent plots were constructed using the ggplot2 (v.3.2.0) and the ggpubr (v.0.2.1) package in R.

Diffusion Maps

To construct the diffusion maps (Coifman and Lafon, 2006), pre-processed data were further processed similarly to the above UMAP, except that only seven variables were selected (see link in Data and Software Availability for complete list). These seven variables were selected from the distinguishing features identified by both the supervised XGboost classifier and the unsupervised UMAP. First, the six features from the SHAP value analysis were chosen. However, ''Time since Track Start'' and ''Track Duration'' are partially redundant. While ''Track Duration'' indicates the stability of the microcluster on the surface of the T cell, ''Time since Track Start'' simply indicates the order the microclusters appear along this track, and therefore has less physical meaning. Thus, ''Track Duration'', was selected and ''Time since Track Start'' was excluded. In addition, ''Mean Intensity'' was selected over ''Median Intensity'', since the former is a more common analysis metric. Finally, ''Area'' and ''Speed'' were also selected, as they encode independent information that have not been captured by the initial 5 features; for instance, surface units with the same volume can have different shapes, thereby lending to different surface area.

To conserve computational resources, a subset of 8,000 surface modules were randomly sampled from every group. Data from four core groups, including stimulated blast T cells, stimulated naïve T cells, resting naïve T cells, and resting blast T cells, were pooled and used to build the diffusion maps using the diffusionMap (v.1.1.0.1) package in R with default parameters. Nystorm out-of-sample extension was then used to estimate the diffusion coordinates of surface modules of other groups. All subsequent plots were constructed using the ggplot2 (v.3.2.0) and the ggpubr (v.0.2.1) package in R.

Pseudo-Energy Plot

For each group, the diffusion coordinates of the 8,000 sampled surface modules were used to build its pseudo-energy plot. The local probability density, $\widehat{p}(\overrightarrow{x})$, at each data point on the diffusion map was estimated using the ks-package (1.11.5) in R. The density values from the diffusion map embedding coordinates can be used to derive Free Energy Surface as follows:

$$\beta G(\overrightarrow{x}) = -\ln\widehat{p}(\overrightarrow{x}) + const$$

Where $\beta = \frac{1}{k_B T}$; G is the Gibbs free energy, and $\widehat{p}(\overrightarrow{x})$ is the estimated local probabilistic density on the diffusion map. Here, we used $-\ln\widehat{p}(\overrightarrow{x})$ as a pseudo-energy since we cannot experimentally determine the constant term, but this pseudo-energy should be linearly related to the Gibbs free energy and thus gives a good representation of the free energy surface (Ferguson et al., 2010).